Received: 11 January 2022 | Revised: 7 May 2022 | Accepted: 9 May 2022

DOI: 10.1002/apj.2786

RESEARCH ARTICLE

Asia-Pacific Journal of Chemical Engineering | Curtin University | WILEY

Experimental investigation of pore structure during high sodium coal ash sintering with and without calcium oxide additive through XCT technology

Hao Fang | **Zhaowen Wang** | **Jiawei Luo** | **Mengting Ji** | **Hao Zhou**

State Key Laboratory of Clean Energy Utilization, Institute for Thermal Power Engineering, Zhejiang University, Hangzhou, People's Republic of China

Correspondence
Hao Zhou, State Key Laboratory of Clean Energy Utilization, Institute for Thermal Power Engineering, Zhejiang University, Hangzhou, Zhejiang 310027, People's Republic of China.
Email: zhouhao@zju.edu.cn

Funding information
National Natural Science Foundation of China, Grant/Award Number: 52036008

Abstract

This article investigates the evolution of morphology and pore structure during sintering at 1200°C for a high sodium coal ash, with and without using a calcium oxide additive. The effect of different proportions of calcium oxide additive was studied. The ratios of height and area of samples were calculated, and representative sintering time points of morphological changes were captured. Meanwhile, frequencies of diameter, pore numbers, and porosities were obtained by processing images. The maximum ratio of height and area reached at 15 min, 4 min, and 10 min for the sintering process of coal ash sample without additive, with 5% and 10% CaO, proving that CaO accelerates the sintering process. In comparison, the maximum porosities were 52.4%, 39.5%, and 47.0% for sintering samples after 10 min, 6 min, and 40 min. Besides, X-ray diffraction analysis of the minerals of the condensed white matter was conducted.

KEYWORDS

calcium oxide additive, CCD digital image technique, high sodium coal, pore structure evolution, X-ray computed microtomography

1 | INTRODUCTION

According to the BP Statistical Review of World Energy 2020, the total energy consumption of the world has been increasing while the total primary energy reached 5.839×10^{17} kJ in 2019.[1] Due to its abundant reserves and low cost, coal-fired power plants will still be one of the essential sources of power production in the foreseeable future. Unfortunately, the coal-fired boiler is often accompanied by scaling, slagging, erosion, heat transfer surface wear, and other problems. Among them, ash slagging is one of the most important problems, leading to the corrosion of water wall tubes and the reduction of heat transfer efficiency.[2–4] It has been reported that slagging behavior contains three stages, while sintering behavior is the major stage of slagging.[5] Consequently, sintering process optimization is an important research point that needs to be solved. Many scholars investigated the sintering behavior of high sodium coal ash for abundant reserves and wide distribution.[6–8] And some researchers[9–12] mentioned that additive technology was an effective as well as an economical method to alleviate these problems. With the additives, the coal ash properties vary with variations of minerals, and then the sintering and melting mechanism will also change.[6] Many kinds of literature focused on the influence of calcium on the fusion characteristics of coal ash with the high-temperature melting point. Russell et al.[13] considered that CaO played an effective role in reducing slag melting point. Zhou et al.[14] researched the influence of

CaO additive on the sintering of ash, reporting that CaO can inhibit the sintering and melting behavior of fly ash. The content of the additive is a significant influence factor on the sintering of coal ash. Dai et al.[15] reported that low-temperature eutectic reacting from the high content of CaO with Fe_2O_3 in the ash resulted in the liquid state of ash. Song[16] and Liu[17] investigated the coal ash melting variations first decreased and then increased with CaO addition, which was related to the content of silicon and its mineral formation. When the content of CaO increased to a certain extent, the silicon transformed from minerals with a lower melting point to those with a higher melting point. It means that a high proportion of CaO additive has a positive effect on reducing the possibility of slagging in the furnace, mixed with the coal before combustion.

Some literature[18–21] stated that pore structure in sintering ash shortened the service life of devices and affected the heat conduction, which has attracted extensive attention of many researchers. At the same time, image processing technology is gradually rising as an analysis method to reveal the internal pore structure. In the previous investigation, 2D image analysis and processing methods were utilized to study the pore structure of ash sintering.[22,23] X-ray computed microtomography (XCT), a 3D reconstruction technology based on actual geometrical structure, was widely applied to analyze the structure lately.[24–34] Hajizadeh et al.[24] applied the method to analyze the pore structure based on the data from XCT. Ranut et al.[25] and Bodla et al.[26] analyzed the pore microstructure and evaluated the thermal conductivity for aluminum foam by high-resolution X-ray microtomography. Zhou et al.[35] applied XCT technology to reconstruct the volume and carried out the porosity of foundation materials in the molten salt tank for the thermal engineering storage system. However, few researchers explored the pore structure evolution process over time during high sodium coal ash sintering through XCT, a high precision method based on the real structure.

This article aims to research the pore structure evolution during high sodium coal ash sintering over sintering time by digital image processing and XCT-based methods. And the effect of adding different ratios of calcium oxide additives was investigated. Additionally, established on XCT technology, pore structure was reconstructed, and pore parameters, including frequencies of pore size, numbers, and porosities, were calculated over sintering time. For the explanation of pore formation, condensed matters in pores were characterized by X-ray diffraction analysis (XRD). The investigations provide the basis for the combustion and utilization of high sodium coal and the safety of power stations, which has important significance.

2 | EXPERIMENT AND METHODS

2.1 | Materials

The ZD coal from Xinjiang province, a kind of lignite coal with high sodium, was researched as the experimental object in this article, the properties of which, including ash composition, ultimate and proximate analysis, and ash fusion temperature, were listed in Table 1. According to ASTM D2795-95 and ASTM D1857-87, ash composition and ash fusion temperature were measured, respectively.[36] Following the ASTM D3176, we applied the elemental analyzer to determine the ultimate analysis and used a muffle furnace to

TABLE 1 Fuel properties

Fuel	ZD coal
Proximate analysis (wt%)	
M_{ad}	15.6
A_{ad}	12.3
V_{ad}	32.79
FC_{ad}	52.91
Ultimate analysis (wt%)	
C_{ad}	64.07
H_{ad}	3.58
N_{ad}	0.65
S_{ad}	0.18
O_{ad}	19.22
Ash fusion temperature (°C)	
IT	1101
ST	1163
HT	1172
FT	1178
Ash composition (wt%)	
SiO_2	27.43
Al_2O_3	14.50
Fe_2O_3	4.26
CaO	27.46
MgO	2.90
K_2O	0.33
Na_2O	7.6
TiO_2	0.87
Cl	10.72

characterize the proximate analysis on the basis of ASTM D 3174.[37]

In order to prepare ash, pulverized coal was first heated for dry oxidation at 823 K,[38] following the rule of ASTM E1755. It could be seen from Table 1 that coal ash has a higher content of CaO (27.46%) and Na_2O (7.60%), compared with other coals.[39,40] Some researchers[13,14] argued that the coal ash melting variations first decreased and then increased with the increment of CaO additive. It is of great significance to study the effect of CaO content on the sintering of ZD coal ash. The ZD coal ash without additive and with 5% and 10% CaO was tested in this paper, so as to explore the influence of different proportions of CaO. As for the conditions with additive, coal and calcium oxide were ground and mixed in a mortar. Before the sintering experiment, 4 g of sample was put in a square mold with 15 mm × 15 mm, and then maintained the pressure at 5 MPa for 3 min to depress the mold every time. Three samples were prepared to repeat the experiment for each condition.

2.2 | Sintering experimental section

2.2.1 | Experimental setup

A 12-kW controllable and programmable electric furnace was applied for sintering experiments in this paper. Figure 1a demonstrated the experimental system including temperature control system, programmable electric heater system, charge-coupled device (CCD) monitoring system, sample position control system, insulating system, and digital display meter connected with a thermocouple. The details and components of the CCD monitoring system were displayed in Figure 1b, which was applied to monitor the appearance change during

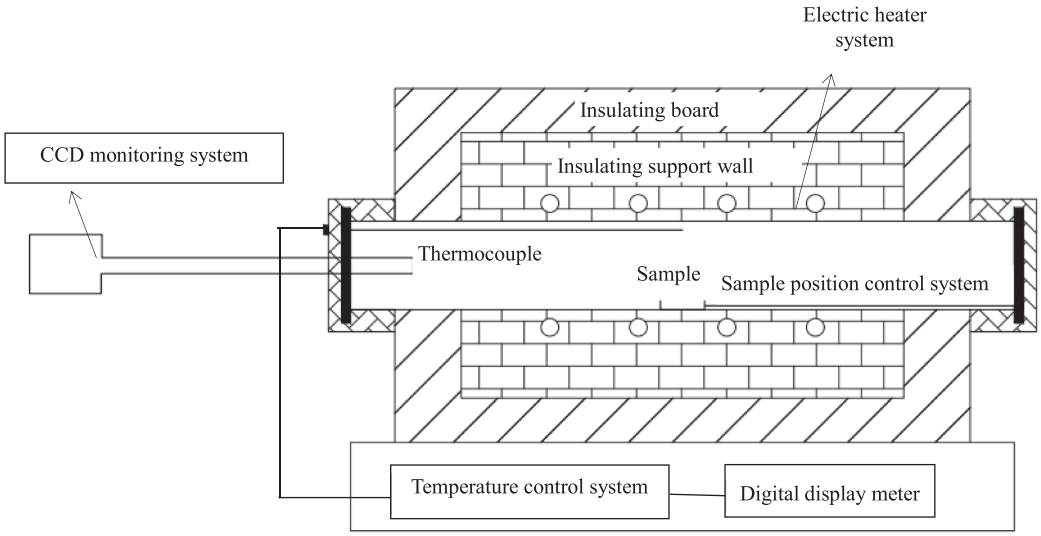

(a) Whole experimental setup

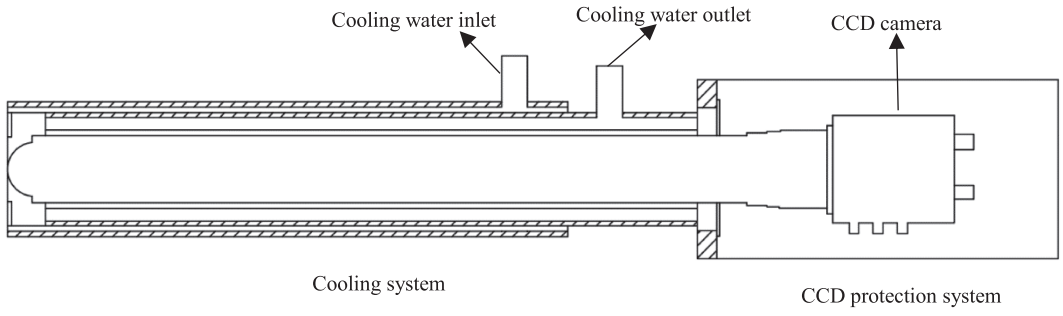

(b) CCD monitoring system

FIGURE 1 Schematic diagram of whole experimental setup (a) and details of CCD monitoring system (b)

the sintering. The CCD monitoring system consisted of a cooling system and camera protection system, recording 24-bit images of sample shapes. Before the experiment, we preheated the tube furnace to 1200°C where ZD ash began to melt, and then the CCD monitoring system started recording. After that, the sample was placed at the center of the device with the sample position control system. The sintering process of the sample was observed by the CCD monitoring system while representative time points of morphological change were recorded. Moreover, we obtained the sintered samples after sintering for different representative times and cooled them with liquid nitrogen to maintain pore structures.

2.2.2 | Digital image theory by CCD

We monitored the appearance changes of the sample in the sintering process through the CCD monitoring system. A digital image processing method was adopted, seen in Figure 2, to analyze the image through CCD recording and calculate the ratio of height and area.

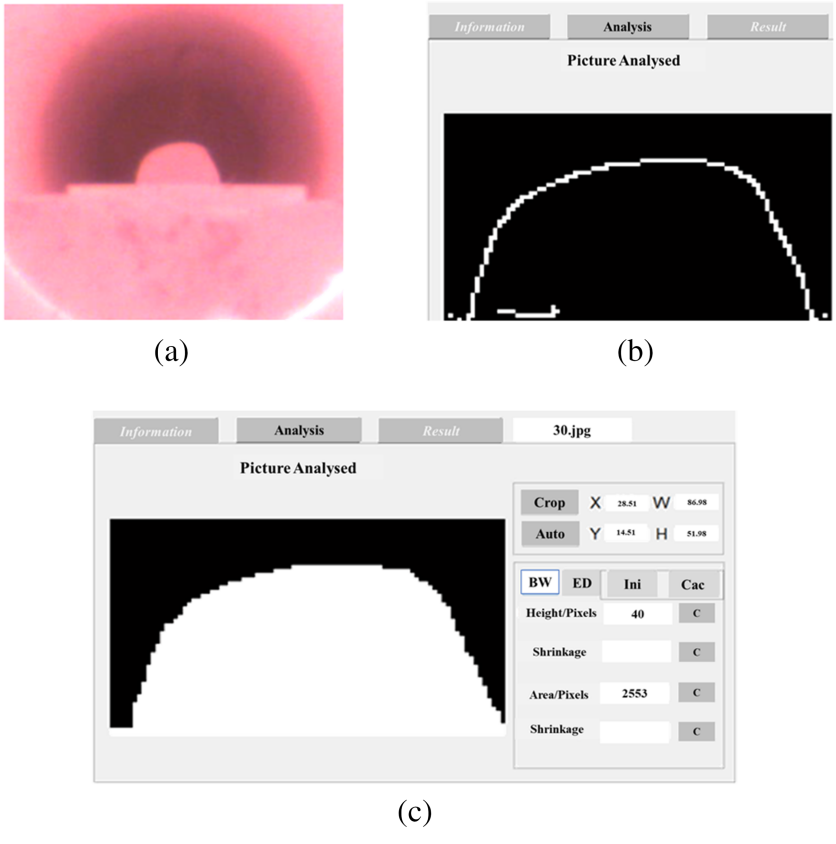

FIGURE 2 The digital image processing of the ash sample during sintering from CCD monitoring system: (a) original image; (b) edge image; (c) binarization image

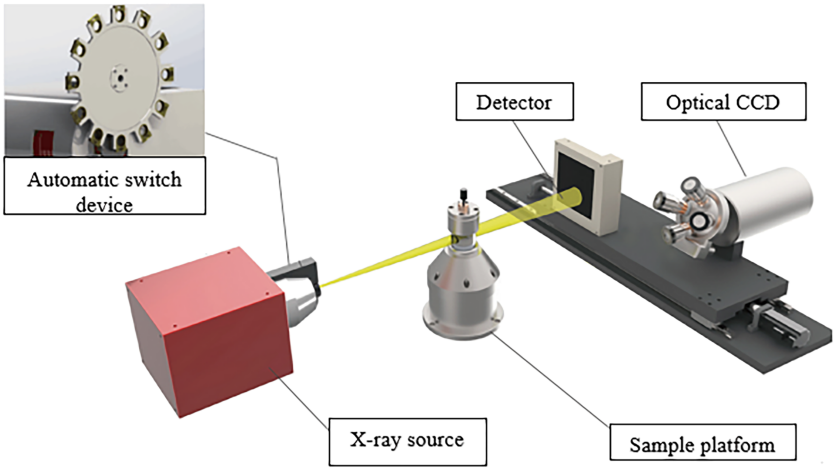

FIGURE 3 Diagrammatic sketch of 4000 Nano-voxel X-ray three-dimensional microscope

Figure 2a displays the 24-bit image of samples captured by CCD. For extracting the boundary of the sample, we applied the edge extraction algorithm on the basis of MATLAB software while the edge image was exhibited in Figure 2b. In this way, the number of high pixels could be gained. The rate of ash sample height can be calculated by the formula:

$$\rho_1 = H/H_1 \quad (1)$$

where ρ_1 represents the ratio of real-time sample height to the initial height; H is the number of pixels of the real-time height during the sintering process, while H_1 is the number of pixels of the original height. In addition, the image in Figure 2a was also binarized, which can be seen in Figure 2c. Therefore, the ratio of the real-time area to the initial area could be calculated by the formula:

$$\rho_2 = S/S_1 \quad (2)$$

where S and S_1 represent the number of pixels of the real-time area and initial area, during the sample sintering process.

TABLE 2 Parameter information about the XCT test for the samples

Item	Value
Voltage (kV)	200
Current (μA)	350
Exposure time (s)	0.62
Source to sample distance (mm)	209
Source to detector distance (mm)	840
Pixel size (μm)	36

2.3 | X-ray 3D computed microtomography

2.3.1 | Testing equipment and conditions

A 4000 Nano-voxel series X-ray three-dimensional microscope instrumentation was used to reconstruct the pore structure and counted the pore parameters of sintered samples with different sintering times, displayed in Figure 3. As we can see, the XCT experimental device consisted of a flat detector, sample platform, open 225 kV X-ray source, optical coupling CCD and automatic switch

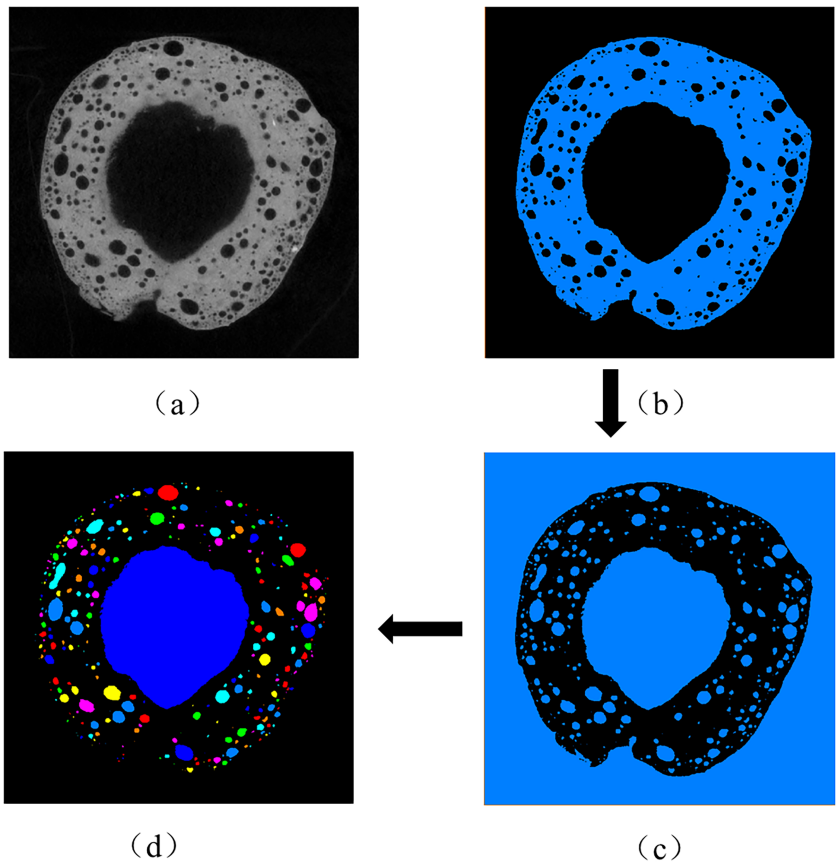

FIGURE 4 The image processing based on XCT theory. (a) Original 16-bit gray-scale slice, (b) image after binarization (blue: solid phase; black: pores), (c) pore phase image, and (d) image of pores in sample after segmenting and removing the boundary air phase

device, which had the ability to choose the suitable filter. Table 2 listed XCT equipment parameter information. The sample platform was 290 mm and 804 mm away from the detector and X-ray source. Besides, the tested sample was rotated 360° at 0.25 angle intervals, and we collected 1440 pieces of radiographs.[41] Considering the appropriate scanning accuracy and acceptable computational amount, we set the resolution of CT

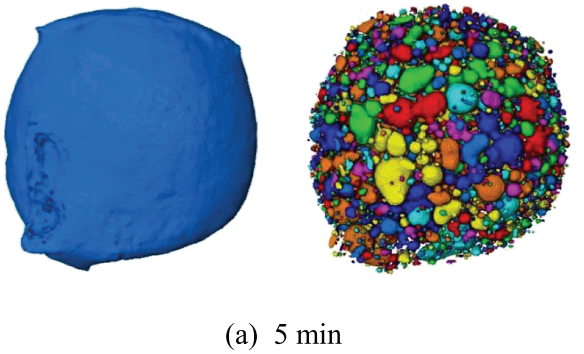

(a) 5 min

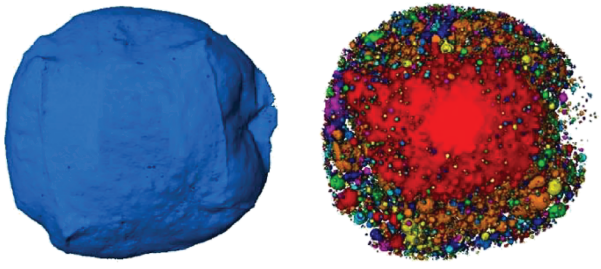

(b) 10 min

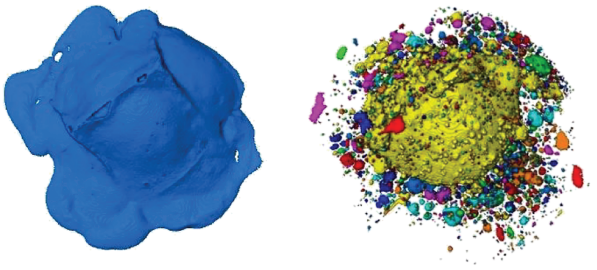

(c) 15 min

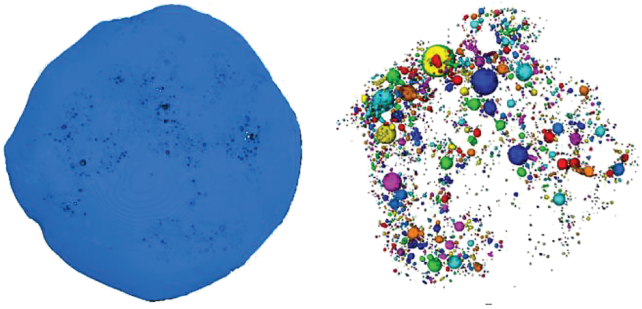

(d) 25 min

FIGURE 5 Rendering volume of the samples and pore distributions for the coal working condition after different sintering time

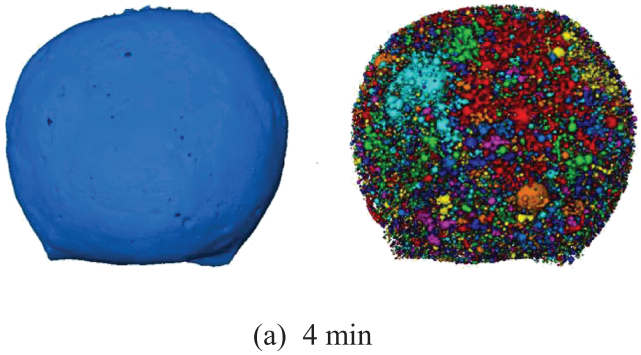

(a) 4 min

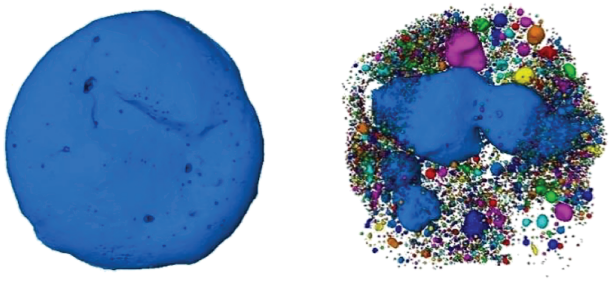

(b) 6 min

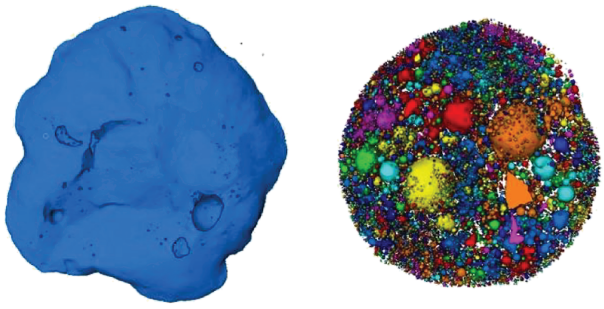

（c）8 min

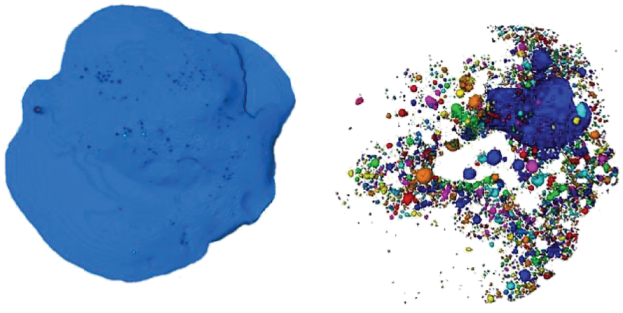

（d）12 min

FIGURE 6 Rendering volume of the samples and pore distributions for the 5% CaO working condition after different sintering time

images at 36 μm. By processing these CT images, the pore structure was reconstructed, and pore parameters were calculated out.

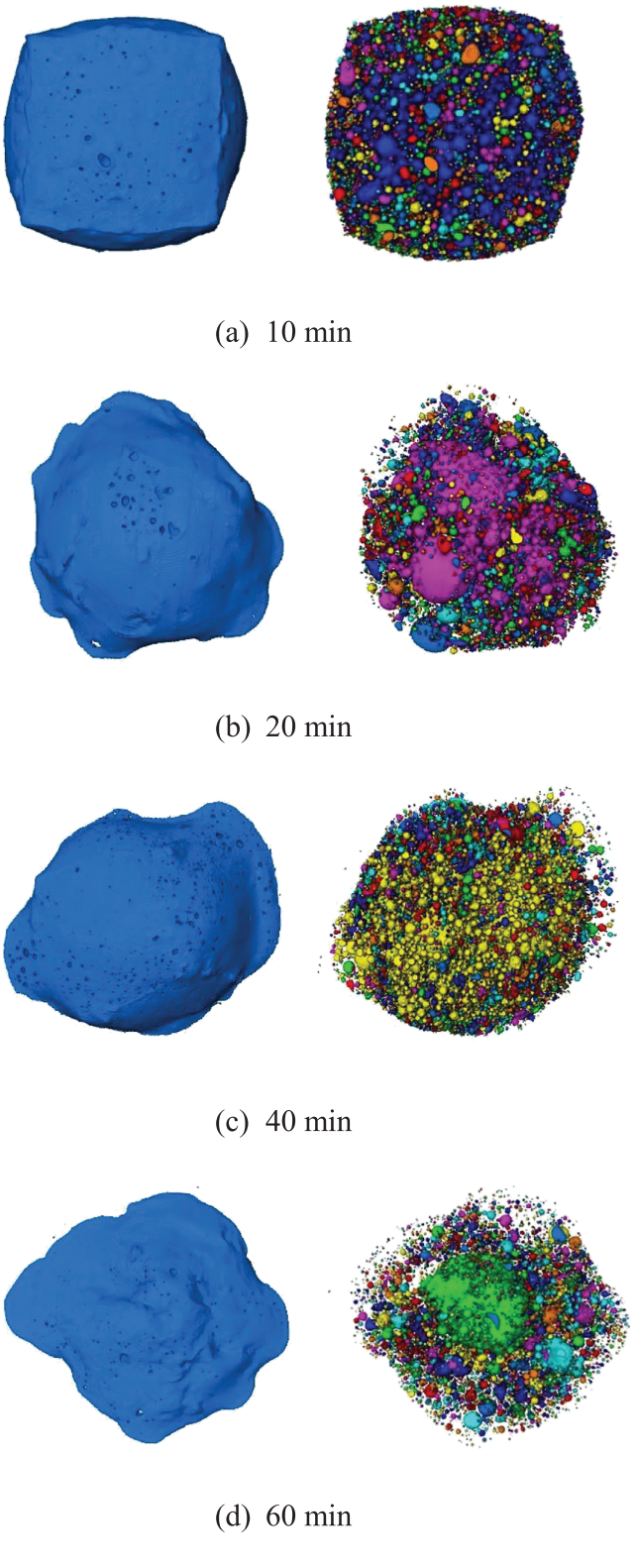

FIGURE 7 Rendering volume of the samples and pores in the samples for 10% CaO working condition after different sintering time

2.3.2 | Statistical methods for the pore parameters

The pore structure can be reconstructed and analyzed through stacking CT images. It can be comprehended from Beer–Lambert law[42] that the X-ray absorptivity of solid and air pores is largely different because of the different atomic structures. An initial 16-bit density grayscale CT image was shown in Figure 4a.[43] The threshold algorithm was applied[44] to distinguish the sample solid phase and pores in Figure 4b. The value of each voxel outside the threshold is 0, which is the pore phase shown in black in Figure 4b, and the others are 1. To extract the pores, we carried out the Boolean algorithm to obtain Figure 4c, during which we transformed each voxel with value 0 (pore phase) to 1. Ultimately, the volume connected to the border was removed, and pores in the sample were separated into individuals. Thus, the separated pores were shown in Figure 4d while the pore structure was gained. In regard to the volume reconstruction, we accumulated 2D CT images along the load direction,[45,46] and the reconstructing volumes of the sample and pores at specific sintering time were shown in Figures 5–7. Meanwhile, the pore numbers, frequencies of the pore diameters, and porosities were obtained.

The porosity was computed by Equations (3) and (4).

$$\varphi = V_s/V \tag{3}$$

$$\rho = 1\text{-}V_s/V \tag{4}$$

where φ is the proportion of sample solid in the total domain while ρ is porosity; V is the volume of the whole sample, while the subscripts "s" represent the solid phase. The contiguous pores were segregated to acquire equivalent diameters statistics of pores, and then the

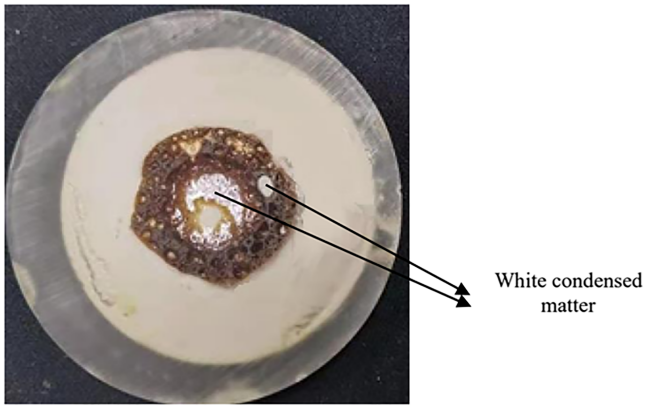

FIGURE 8 Schematic diagram of cross section and internal structure of sintered sample

equivalent diameter, D, was calculated out by the Equation (5):

$$D = \sqrt[3]{\frac{6V_1}{\pi}} \tag{5}$$

where V_1 stands for the volume of a certain pore.

2.4 | Analytical method for condensed matter in pores

To investigate the mineral phase of white condensed matter in the pores, we applied the X-ray diffraction (XRD) analytical method. Samples were cured with resin and then sliced to obtain the white condensed matter in pores. Figure 8 is the sample cutting, from which we took the condensed matters out and ground them for XRD. The XPERT-3 diffractometer system was applied for XRD, including Pixel 1d universal matrix detector, Cu anode X-ray tube, and PW3050/60 goniometer. The operational parameters during the scanning of XRD are listed in Table 3.

TABLE 3 Operational parameters during scanning in XRD analysis

Item	Value
Scan type	Continuous
Voltage (kV)	40
Current (mA)	40
Increment of each step (°)	0.026
Counting time per step (s)	30
Source to detector distance (mm)	840
Scanning range	10°–80°

3 | RESULTS AND DISCUSSION

3.1 | Appearance change process

Figure 9 displayed the sample appearance of ZD coal ash without additive, with 5% CaO and 10% CaO after different sintering times. For the samples without additive, the color deepened while the shape changed with the increase of sintering time which can be seen from Figure 9a. It is evident that the sintered sample at 5 min became round and blunt while the top bulged, indicating that pore appeared. With the sintering time up to 10 min, the sample expanded obviously and the volume increased. The cross-sectional area increased while the color deepened after 15 min sintering time. Finally, at

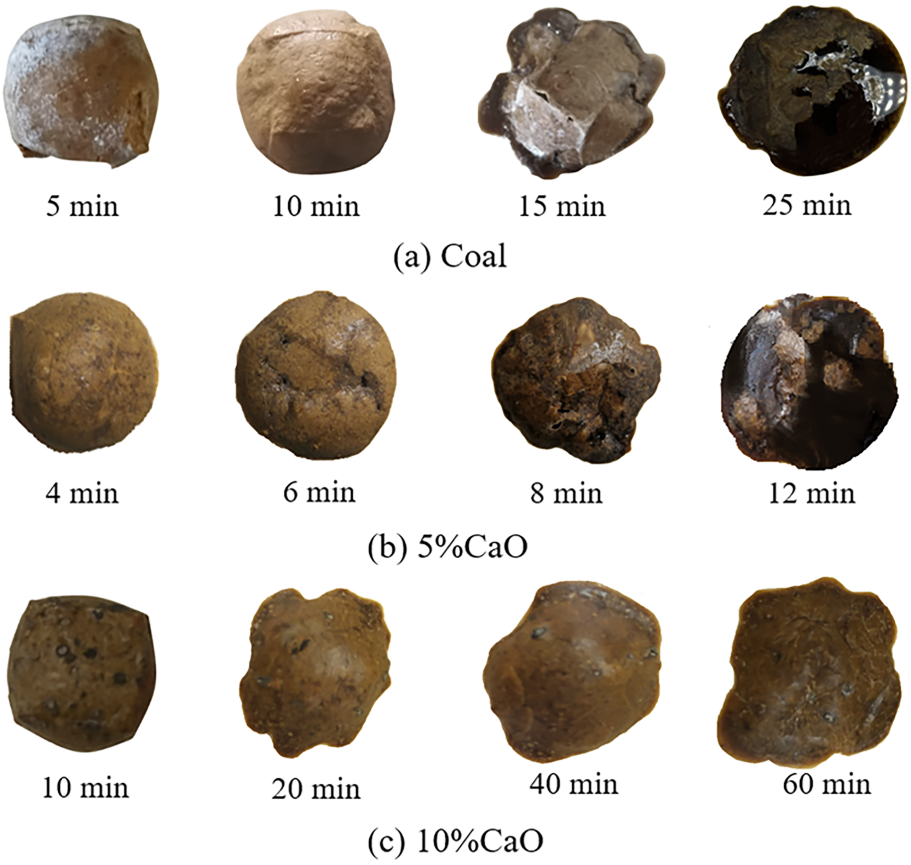

FIGURE 9 Appearance photos of the ash samples sintered with different times for coal, 5% CaO, and 10% CaO

25 min, the height of the sample dropped to a low level, and the color reached the deepest, which indicated that the liquid phase composition increased with the decrease of porosity. What is more, a lot of holes were observed on the surface at 25 min, illustrating that bubbles moved to the surface and escaped. The morphology evolution process of the condition with 5% calcium oxide additive is similar to that of the coal condition. By contrast, the time reached the final state with dark color and stable low height was significantly shortened, which indicated that 5% CaO additive promoted the sintering and melting of high sodium coal ash. Interestingly, after adding 10% CaO, as shown in Figure 9c, the morphology evolution of high sodium coal ash during the sintering process changed significantly. The evolution speed of the sample morphology was so slow that the sample still had a certain height after sintering for 60 min. And the color of the sample was not deepened. After sintering for 20 min, the height and morphology variations were no longer apparent. In a word, adding 10% calcium oxide additive had a strong inhibition effect on the sintering of high sodium coal ash.

3.2 | Height and area changes through CCD

Based on digital image processing technology, the changes in height and area of ash samples during the sintering process were monitored. The variation curve of the ratio of height and area with sintering time was displayed in Figure 10. As can be seen from Figure 10, the sample shrunk with the decrease of height and area obviously in the beginning. Afterward, the height and area of the sample rapidly increased to the highest point of curves. Then the curves declined at a fast rate. In the end, the sample reached a stage where the height and area changed very slowly. It could be found in Figure 10 that the time reaching the highest point of curves under three conditions is 15 min, 4 min, and 10 min. That is to say, adding calcium oxide additive is conducive to shortening the time to reach the highest point, while the addition of 10% CaO inhibited the sintering process of high sodium coal ash. In consequence, the CaO additive promoted the formation of internal pores, that is, bubbles in the early sintering stage.

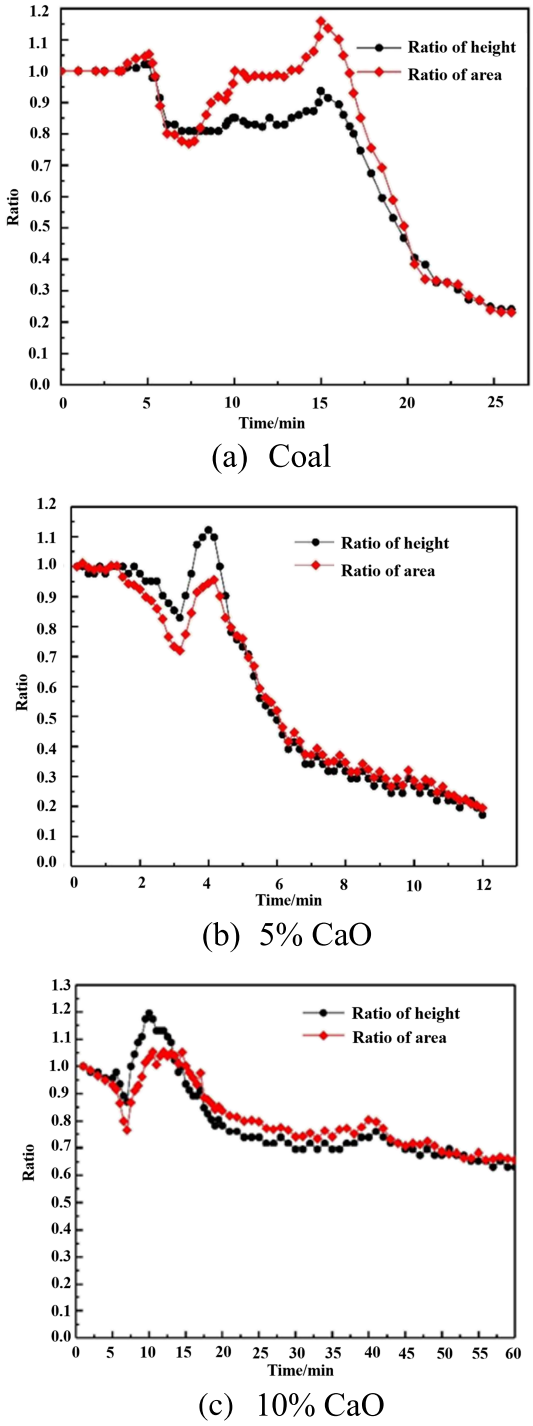

FIGURE 10 Ratio of height and area for the sample during the sintering. (a) ZD coal, (b) 5% CaO, and (c) 10% CaO

3.3 | Pore structure reconstruction and parameters statistics by XCT

For the investigation of pore structure evolution, we gained the sintering time point when obvious morphological change, observed from the curves in Figure 10. We reconstructed the pore structures of samples in Figures 5–7, while the pore parameters, including frequency of pore diameters, porosity, and pore number, were displayed in Figures 11 and 12.

We can observe from Figure 11 that the total pore number in the samples decreased rapidly with sintering

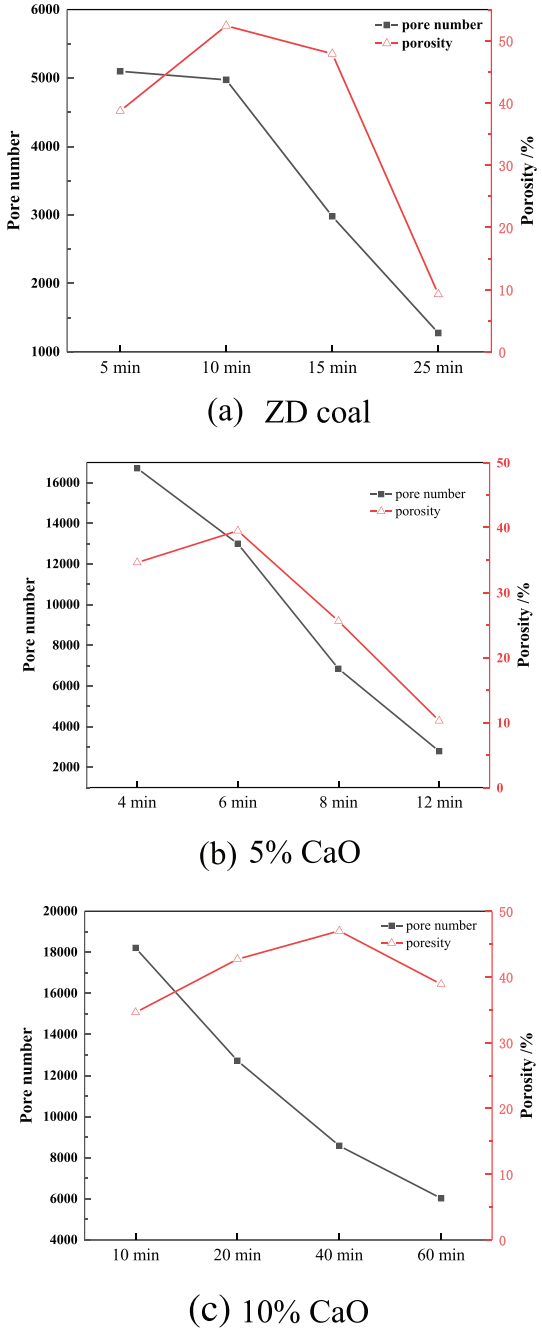

FIGURE 11 Pore numbers and porosity of different sintering time during the sintering process for high sodium coal ash without and with 5% and 10% CaO. (a) ZD coal, (b) 5% CaO, and (c) 10% CaO

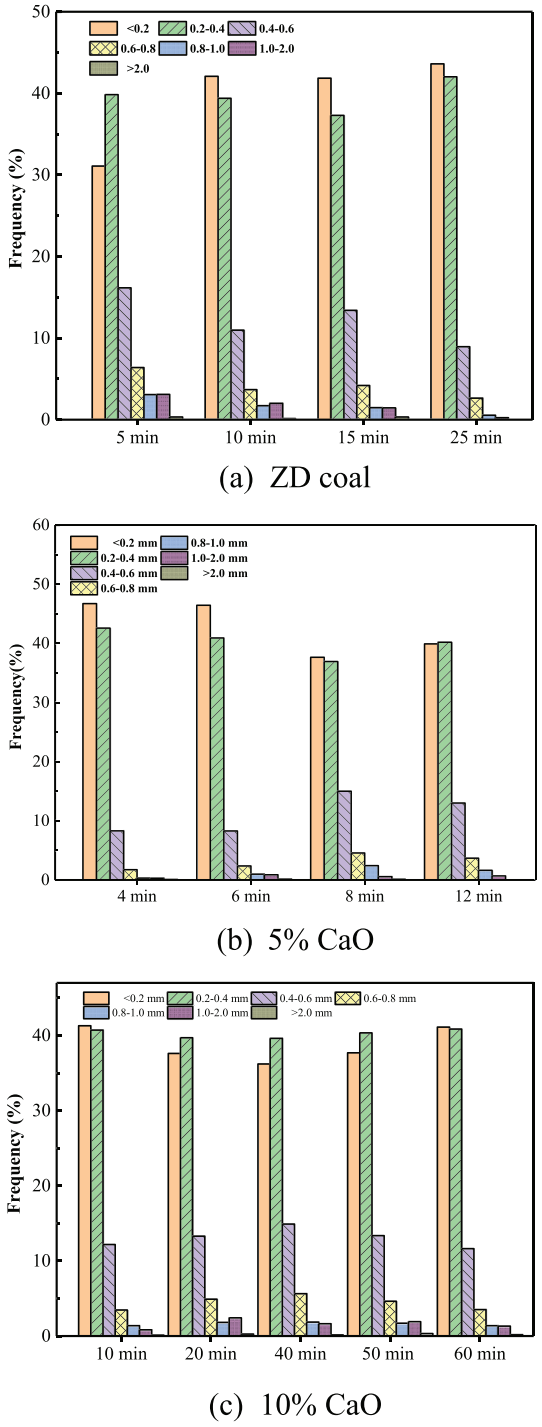

FIGURE 12 Frequency of equivalent pore diameters of samples with different sintering time for three experimental conditions. (a) ZD coal, (b) 5% CaO, and (c) 10% CaO

time. In the early sintering process, the pore number achieved the maximum on account of the formation of great plenty of fine bubbles. With the further enhancement of the sintering degree, the pore number decreased quickly on account of the coalescence and escape of bubbles. The pore numbers in the samples without additive were less than that with calcium oxide, which indicated that the addition of CaO promoted the generation of bubbles. Also, Figure 11 showed that porosity firstly increased and then decreased with sintering time. When sintering for 10 min, 6 min, and 40 min, the porosities of ZD coal without and with 5% CaO and 10% CaO additives were 52.4%, 39.5%, and 47.0% respectively. For ZD coal without and with 5% CaO, the porosity reached a lower value (less than 10%) at final while the

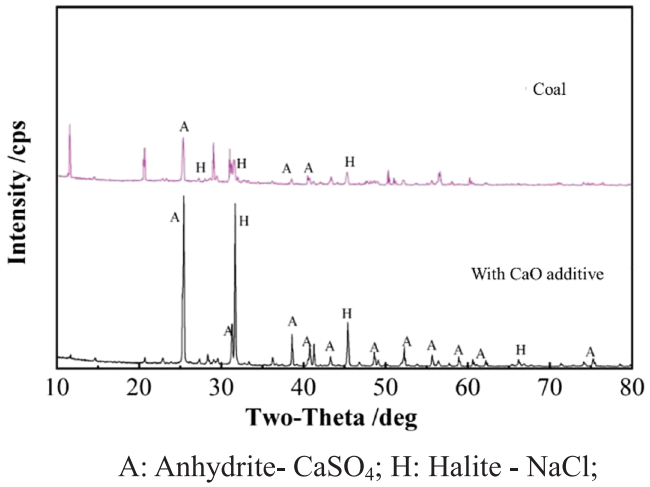

FIGURE 13 Mineralogical compositions of condensates in pores of sintered coal ash without and with CaO additive

porosity of 10% CaO condition changed not obviously, ranging from 34.6% to 47.0%. To analyze the evolution of pore structure in the sintering process, we split the pores into groups according to the pore diameter while the frequency of each group is shown in Figure 12a–c. It is observed that the frequencies of diameter less than 0.4 mm were higher than 70% in all samples. The frequencies of the small pores with a diameter less than 0.4 mm first decreased and then increased, which also confirmed the coalescence of small bubbles in the early stage and the rupture of large bubbles in the later stage.

3.4 | Porous structural evolution mechanism

In light of the results in Sections 3.2 and 3.3, a great many small pores were produced at the early stage while the pore number rose to the maximum rapidly. With the progress of sintering, the porosity increased with the coalescence and expansion of pores in samples. Furthermore, the further melting and sintering of the sample, that is, the appearance of the molten phase and the gas–liquid two-phase state, promoted the escape of bubbles, resulting in decreased pore number and porosity. Finally, pore parameters and the height of the ash sample decreased to a stable minimum due to the reduction of gas production, which was in balance with the bubble escape.[47] By reason of the inhibition of high sodium coal combustion by adding 10% CaO additive, the pore parameters of samples changed slowly with sintering time.

In order to explore the mechanism of pore structure generation and change, we characterized the main mineral phases of white condensate in the sample pores in Figure 13, which were halite and anhydrite. With the addition of calcium oxide, a great number of anhydrite peaks increased in the XRD pattern of the condensates in the pores. The experimental results showed that because of the high sodium and calcium content of ZD coal, the pore structure is generated accompanied by the formation and gasification of anhydrite and the volatilization of alkali chlorides. The addition of CaO promotes the formation and gasification of $CaSO_4$, thus promoting the generation of pores.

4 | CONCLUSION

Pore structure evolution during sintering of high sodium coal ash was studied in a programmable horizontal furnace. The effect of adding calcium oxide with different proportions on the pore structure evolution during the coal ash sintering process was also investigated. Based on the CCD monitoring system and digital image processing technology, the appearance of the sintering process was observed while shape parameters, including height and area, were calculated. XCT technology is utilized to rebuild the pore distribution and calculate the pore parameters. Results are shown as follows:

1. The sample underwent a shrinkage process and then expanded rapidly with area and height increasing to the maximum. Afterward, the ratio of area and height decreased and finally reached a stable state. The addition of calcium oxide shortened the time to reach the highest point of height and area. The results suggested that 5% CaO promoted the coal ash sintering while the addition of 10% CaO could inhibit the sintering process.
2. With the addition of 5% CaO, the ash reached the state with a stable low height and porosity more quickly than without additive condition. However, adding 10% CaO, the ash sample had a high porosity of 39% after 60 min while the height and area curves changed slowly from 20 min to 60 min sintering time.
3. The mineral composition of condensed matter in pores was NaCl and $CaSO_4$, showing that pore structure generated for the formation and gasification of anhydrite and the volatilization of alkali chlorides. With the addition of CaO additive, the time reaching the maximum height was obviously advanced while pore numbers increased significantly due to the promotion of anhydrite formation.

ACKNOWLEDGEMENT

This work was supported by National Natural Science Foundation of China (52036008).

CONFLICT OF INTEREST

The authors declare that they have no competing financial interests.

ORCID

Hao Zhou https://orcid.org/0000-0001-9779-7703

REFERENCES

1. BP. BP statistical review of world energy 2020. Last modified November 2019. Accessed June 2020. http://bp.com/statisticalreview
2. Arvelakis S, Folkedahl B, Dam-Johansen K, Hurley J. Studying the melting behavior of coal, biomass, and coal/biomass ash using viscosity and heated stage XRD data. *Energy Fuel*. 2006;20(3):1329-1340. doi:10.1021/ef050168b
3. Wang H-F, Harb J-N. Modeling of ash deposition in large-scale combustion facilities burning pulverized coal. *Prog Energy Combust Sci*. 1997;23(3):267-282. doi:10.1016/S0360-1285(97)00010-5
4. Kostakis G. Mineralogical composition of boiler fouling and slagging deposits and their relation to fly ashes: The case of Kardia power plant. *J Hazard Mater*. 2011;185(2–3):1012-1018. doi:10.1016/j.jhazmat.2010.10.006
5. Zhou H, Zhou B, Dong K, Ding J-Z, Cen K-F. Research on the slagging characteristics of easy to slagging coal in a pilot scale furnace. *Fuel*. 2013;109:608-615. doi:10.1016/j.fuel.2013.03.044
6. Li J-B, Zhu M-M, Zhang Z-Z, Zhang K, Shen G-Q, Zhang D-K. Characterisation of ash deposits on a probe at different temperatures during combustion of a Zhundong lignite in a drop tube furnace. *Fuel Process Technol*. 2016;144:155-163. doi:10.1016/j.fuproc.2015.12.024
7. Qi X-B, Song G-L, Song W-J, Yang S-B, Lu Q-G. Effects of wall temperature on slagging and ash deposition of Zhundong coal during circulating fluidized bed gasification. *Appl Therm Eng*. 2016;106(4):1127-1135. doi:10.1016/j.applthermaleng.2016.06.092
8. Lu Y, Wang Y, Xu Y, Li Y, Hao W-X, Zhang Y-F. Investigation of ash fusion characteristics and migration of sodium during co-combustion of Zhundong coal and oil shale. *Appl Therm Eng*. 2017;121:224-233. doi:10.1016/japplthermaleng.2017.04.062
9. Shi W-J, Laabs M, Reinmöller M, et al. In-situ analysis of the effect of CaO/Fe_2O_3 addition on ash melting and sintering behavior for slagging-type applications. *Fuel*. 2021;285:119090. doi:10.1016/j.fuel.2020.119090
10. Zhou H, Luo Z-H, Liu D, Ma W-C. Effect of biomass ashes on sintering characteristics of high/low melting bituminous coal ash. *Fuel Process Technol*. 2019;189:62-73. doi:10.1016/j.fuproc.2019.01.017
11. Zhou H, Luo J-W, Wang Z-W, Ji M-T, Zhang M-R. Effect of walnut shell ash on pore structure characteristics during Zhundong coal sintering. *Fuel Process Technol*. 2021;221(5):106923. doi:10.1016/j.fuproc.2021.106923
12. Fan H-L, Li F-H, Guo Q-Q, Guo M-X, Zhang M-R. Effect of biomass ash on initial sintering and fusion characteristics of high melting coal ash. *J Energy Inst*. 2021;94:129-138. doi:10.1016/j.joei.2020.11.008
13. Russell NV, Wigley F, Williamson J. The roles of lime and iron oxide on the formation of ash and deposits in PF combustion. *Fuel*. 2002;81(5):673-681. doi:10.1016/S0016-2361(01)00154-5
14. Zhou H, Wang J-Y, Zhou B. Effect of five different additives on the sintering behavior of coal ash rich in sodium under an oxy-fuel combustion atmosphere. *Energy Fuel*. 2015;29(9):5519-5533. doi:10.1021/acs.energyfuels.5b00500
15. Dai B-Q, Low F, De Girolamo A, Wu X-J, Zhang L. Characteristics of ash deposits in a pulverized lignite coal-fired boiler and the mass flow of major ash-forming inorganic elements. *Energy Fuel*. 2013;27(10):6198-6211. doi:10.1021/ef400930e
16. Song W-J, Tang L-H, Zhu X-D, Wu Y-Q, Zhu Z-B, Koyama S. Effect of coal ash composition on ash fusion temperatures. *Energy Fuel*. 2010;24(1):182-189. doi:10.1021/ef900537m
17. Liu B, He Q-H, Jiang Z-H, Xu R-F, Hu B-X. Relationship between coal ash composition and ash fusion temperatures. *Fuel*. 2013;105:293-300. doi:10.1016/j.fuel.2012.06.046
18. Zhu H-B, Zhan W-L, He Z-J, Yun Y-C, Pang Q-H, Zhang J-H. Pore structure evolution during the coke graphitization process in a blast furnace. *Int J Miner Metall Mater*. 2020;27(9):1226-1233. doi:10.1007/s12613-019-1927-1
19. Koyama S, Morimoto T, Ueda A, Matsuoka H. A microscopic study of ash deposits in a two-stage entrained-bed coal gasifier. *Fuel*. 1996;75(4):459-465. doi:10.1016/0016-2361(95)00266-9
20. Llorente M-J, Arocas P-D, Nebot L-G, Garcia J-E. The effect of the addition of chemical materials on the sintering of biomass ash. *Fuel*. 2008;87(12):2651-2658. doi:10.1016/j.fuel.2008.02.019
21. Steenari B-M, Lundberg A, Pettersson H, Wilewska-Bien M, Andersson D. Investigation of ash sintering during combustion of agricultural residues and the effect of additives. *Energy Fuel*. 2009;23(11):5655-5662. doi:10.1021/ef900471u
22. Pang C-H, Hewakandamby B, Wu T, Lester E. An automated ash fusion test for characterisation of the behaviour of ashes from biomass and coal at elevated temperatures. *Fuel*. 2013;103:454-466. doi:10.1016/j.fuel.2012.06.120
23. Rushdi A, Gupta R. Investigation of coals and blends deposit structure: measuring the deposit bulk porosity using thermomechanical analysis technique. *Fuel*. 2005;84(5):595-610. doi:10.1016/j.fuel.2004.09.021
24. Hajizadeh A, Safekordi A, Farhadpour FA. A multiple-point statistics algorithm for 3D pore space reconstruction from 2D images. *Adv Water Resour*. 2011;34(10):1256-1267. doi:10.1016/j.advwatres.2011.06.003
25. Ranut P, Nobile E, Mancini L. High resolution X-ray microtomography-based CFD simulation for the characterization of flow permeability and effective thermal conductivity of aluminum metal foams. *Exp Therm Fluid Sci*. 2015;67:30-36. doi:10.1016/j.expthermflusci.2014.10.018
26. Bodla K-K, Murthy J-Y, Garimella S-V. Microtomography-based simulation of transport through open-cell metal foams. *Numer Heat Transf*. 2010;58(7):527-544. doi:10.1080/10407782.2010.511987
27. Guignot N, King A, Boulard E. Synchrotron X-ray computed microtomography for high pressure science. *J Appl Phys*. 2020;127(24):240901. doi:10.1063/5.000.8731
28. Sket F, Seltzer R, Molina-Aldareguia J-M, Gonzalez C, LLorca J. Determination of damage micromechanisms and

fracture resistance of glass fiber/epoxy cross-ply laminate by means of X-ray computed microtomography. *Compos Sci Technol*. 2012;72(2):350-359. doi:10.1016/j.compscitech.2011.11.025

29. Mihalcea E, Vergara-Hernandez H-J, Olmos L, Jimenez O, Arteaga D, Salgado-Lopez J-M. X-ray computed microtomography characterization of Ti6Al4V/CoCrMo biomedical composite fabricated by semi-solid sintering. *J Nondestr Eval*. 2021;40(1):6. doi:10.1007/s10921-020-00742-w
30. Zhou H, Zhou M, Cheng M, et al. High resolution X-ray microtomography for the characterization of pore structure and effective thermal conductivity of iron ore sinter. *Appl Therm Eng*. 2017;127:508-516. doi:10.1016/j.applthermaleng.2017.08.051
31. Petrasch J, Meier F, Friess H, Steinfeld A. Tomography based determination of permeability, Dupuit–Forchheimer coefficient, and interfacial heat transfer coefficient in reticulate porous ceramics. *Int J Heat Fluid Flow*. 2008;29(1):315-326. doi:10.1016/j.ijheatfluidflow.2007.09.001
32. Ranut P, Nobile E, Mancini L. High resolution microtomography-based CFD simulation of flow and heat transfer in aluminum metal foams. *Appl Therm Eng*. 2014;69(1–2):230-240. doi:10.1016/j.applthermaleng.2013.11.056
33. Ranut P, Nobile E, Mancini L. In microtomography-based CFD analysis of transport in open-cell aluminum metal foams. *J Phys Conf*. 2014;501:012021. doi:10.1088/1742-6596/501/1/012021
34. Zafari M, Panjepour M, Emami M-D, Meratian M. Microtomography-based numerical simulation of fluid flow and heat transfer in open cell metal foams. *Appl Therm Eng*. 2015;80:347-354. doi:10.1016/j.applthermaleng.2015.01.045
35. Zhou H, Wang Z-W, Zhou M-X, Xu J-N. Thermal properties, permeability and compressive strength of highly porous accumulated ceramsites in the foundation of salt tank for concentrate solar power plants. *Appl Therm Eng*. 2019;164:114451. doi:10.1016/j.applthermaleng.2019.114451
36. Dyk J. Understanding the influence of acidic components (Si, Al, and Ti) on ash flow temperature of South African coal sources. *Miner Eng*. 2006;19(3):280-286. doi:10.1016/j.mineng.2005.06.018
37. Kozlov A, Svishchev D, Donskoy I, Shamansky V, Ryzhkov A. A technique proximate and ultimate analysis of solid fuels and coal tar. *J Therm Anal Calorim*. 2015;122(3):1213-1220. doi:10.1007/s10973-015-5134-7
38. Braga R-M, Melo D, Aquino F-M, et al. Characterization and comparative study of pyrolysis kinetics of the rice husk and the elephant grass. *J Therm Anal Calorim*. 2014;115(2):1915-1920. doi:10.1007/s10973-013-3503-7
39. Fan H, Li F, Guo Q, Guo M-X. Effect of biomass ash on initial sintering and fusion characteristics of high melting coal ash. *J Energy Inst*. 2021;94(3):129-138. doi:10.1016/j.joei.2020.11.008
40. Liang D, Huang J, Zhang Y, et al. Influence of dextrin content and sintering temperature on the properties of coal fly ash-based tubular ceramic membrane for flue gas moisture recovery. *J Eur Ceram Soc*. 2021;41(11):5696-5710. doi:10.1016/j.jeurceramsoc.2021.04.055
41. Wang Z-W, Zhou H, Li Y-W, et al. Experimental study of the pore structure during coal and biomass ash sintering based on X-ray CT technology. *Energy Fuel*. 2021;35(3):2098-2109. doi:10.1021/acs.energyfuels.0c03668
42. Kocsis L, Herman P, Eke A. The modified Beer-Lambert law revisited. *Phys Med Biol*. 2006;51(5):N91-N98. doi:10.1088/0031-9155/51/5/N02
43. Herman P. *Fundamentals of Computerized Tomography*. USA. New York: Springer; 2009 10.1007/978-1-84628-723-7.
44. Sharma A-K, Goldberg I, Graham S-L, Mohsin M. Comparison of the Humphrey Swedish interactive thresholding algorithm (SITA) and full threshold strategies. *J Glaucoma*. 2000;9(1):20-27. doi:10.1097/00061198-200002000-00005
45. Shatokha V, Korobeynikov I, Maire E, Gremillard L, Adrien J. Iron ore sinter porosity characterisation with application of 3D X-ray tomography. *Ironmak Steelmak*. 2010;37(5):313-319. doi:10.1179/030192310X12683045805865
46. Schmidt F, Kühbacher M, Gross U, Kyriakopoulos A, Schubert H, Zehbe R. From 2D slices to 3D volumes: image based reconstruction and morphological characterization of hippocampal cells on charged and uncharged surfaces using FIB/SEM serial sectioning. *Ultramicroscopy*. 2011;111(4):259-266. doi:10.1016/j.ultramic.2010.12.017
47. Balapour M, Rao R, Garboczi E-J, et al. Thermochemical principles of the production of lightweight aggregates from waste coal bottom ash. *J Am Ceram Soc*. 2021;104(1):613-634. doi:10.1111/jace.17458

How to cite this article: Fang H, Wang Z, Luo J, Ji M, Zhou H. Experimental investigation of pore structure during high sodium coal ash sintering with and without calcium oxide additive through XCT technology. *Asia-Pac J Chem Eng*. 2022;17(3):e2786. doi:10.1002/apj.2786